Microwave-excited microplasma thruster with helium and hydrogen propellants

AUTHOR(S):

Takahashi, Takeshi; Takao, Yoshinori; Ichida, Yugo; Eriguchi, Koji; Ono, Kouichi

PHYSICS OF PLASMAS **18**, 063505 (2011)

Microwave-excited microplasma thruster with helium and hydrogen propellants

Takeshi Takahashi,[a] Yoshinori Takao, Yugo Ichida,[b] Koji Eriguchi, and Kouichi Ono[c]
Department of Aeronautics and Astronautics, Graduate School of Engineering, Kyoto University, Yoshida-Honmachi, Sakyo-ku, Kyoto 606-8501, Japan

(Received 19 March 2011; accepted 10 May 2011; published online 23 June 2011)

Microplasma thruster of electrothermal type has been investigated with feed or propellant gases of He and H_2. The thruster consisted of an azimuthally symmetric microwave-excited microplasma source 1.5 mm in diameter and 10 mm long with a rod antenna on axis, and a converging-diverging micronozzle 1 mm long with a throat 0.2 mm in diameter. Surface wave-excited plasmas were established by 4.0-GHz microwaves at powers of $\leq$ 6 W, with the source pressure in the range 0.5–12 kPa at flow rates of 2–70 sccm. The microplasma generation, micronozzle flow, and thrust performance with He were numerically analyzed by using a two-dimensional fluid model, coupled with an electromagnetic model for microwaves interacting with plasmas in the source region. In experiments, the plasma electron density and gas temperature in the microplasma source were measured at around the top of the microwave antenna, or just upstream of the micronozzle inlet, by optical emission spectroscopy with a small amount of additive gases of H_2 and N_2. In the case of He propellant, the Stark broadening of H Balmer-β line and the vibronic spectrum of N_2 2nd positive (0, 2) band indicated that the electron density was in the range $(2-5) \times 10^{19}$ m^{-3} and the gas or rotational temperature was in the range 600–700 K. The thrust performance was also measured by using a target-type microthrust stand, giving a thrust in the range 0.04–0.51 mN, a specific impulse in the range 150–270 s, and a thrust efficiency in the range 2%–12%. These experimental results were consistent with those of numerical analysis, depending on microwave power and gas flow rate. Similar plasma characteristics and thrust performance were obtained with H_2 propellant, where the specific impulse of $\leq$ 450 s was more than 1.5 times higher than that with He, owing to a difference in mass between He and H_2. A comparison with previous studies with Ar propellant [T. Takahashi *et al.*, Phys. Plasmas **16**, 083505 (2009)] indicated that in the presence as well as absence of plasma discharge, the specific impulse was enhanced by more than 3–5 times with light-mass propellants He and H_2 as has been known for large-scale propulsion systems. Thus, it follows that in the microplasma thruster of electrothermal type, the high diffusivity and thermal conductivity of He and H_2 in the microplasma source of high surface-to-volume ratios do not lead to a deterioration of the thrust performance, primarily owing to a more significant thermal energy gain due to elastic collisions between electrons and heavy particles in He and H_2. © *2011 American Institute of Physics*. [doi:10.1063/1.3596539]

I. INTRODUCTION

Small spacecraft has recently attracted increasing attention in space technology to reduce the overall mission costs and increase the launch rates.[1–3] To realize such microspacecraft of $<$ 10 kg, called "nanosatellites," their components have to be miniaturized, including the propulsion system for station keeping and for attitude control. Various microthrusters have been proposed for these applications,[2–6] including micro electric propulsion systems or micro plasma/ion thrusters:[7–27] direct current (DC) microarcjet thruster,[7–9] DC microplasma thruster (MPD),[10,11] micro Hall thruster,[12,13] micro ion thruster,[14–17] and dielectric capillary discharge acceleration[18] using gas fuels; field emission electric propulsion (FEEP)[19] and colloid thruster[20] using liquid fuels; vacuum arc microthruster (VAμT),[21] micro laser-ablation plasma thruster (μ-LPT),[22,23] micro pulsed plasma thruster (μ-PPT),[24,25] and ferroelectric plasma thruster (FEPT)[26,27] using solid fuels. However, millimeter-scale microthrusters have not yet been well established until now.

We have developed a mm-scale microplasma thruster of electrothermal type using azimuthally symmetric microwave-excited microplasmas,[28–34] consisting of a microplasma source and a micronozzle as shown in Fig. 1. The microplasma source is made of a dielectric chamber covered with a metal grounded, having a metal rod antenna on axis covered with a dielectric envelope, which produces high temperature plasmas at around atmospheric pressures. The micronozzle concerned is a converging-diverging type, which converts high thermal energy of plasmas into directional kinetic energy of supersonic plasma flows to obtain the thrust. The microwave power employed would be limited to $<$ 10 W, taking into account the electric power generated by solar cell panels installed on the microspacecraft

[a]Electronic mail: rainbowmd81@gmail.com.
[b]Present address: Toyota Motor Corporation, Toyota-shi, Aichi 471-8571, Japan.
[c]Electronic mail: ono@kuaero.kyoto-u.ac.jp.

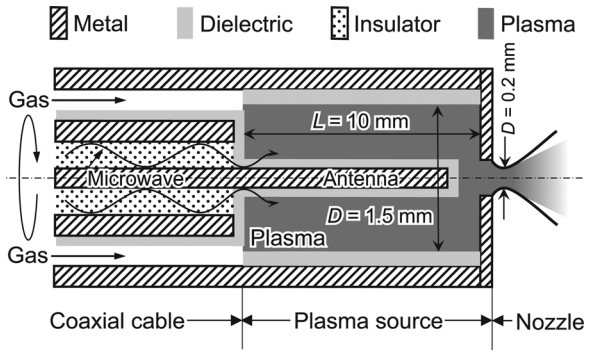

FIG. 1. Schematic of the microplasma thruster using azimuthally symmetric microwave-excited microplasmas, consisting of a microplasma source with a rod antenna on axis and a converging-diverging (Laval) micronozzle. Here, the microplasma source is ~ 1.5 mm in diameter and ~ 10 mm long, and the micronozzle is ~ 1 mm in length, having a throat ~ 0.2 mm in diameter.

concerned. The major feature of our system is that discharges can be established relatively easily over a wide pressure range by surface waves excited around the dielectric envelope of the antenna on axis,[35–38] where microwaves penetrate into the plasma along the plasma-dielectric interfaces even in the overdense mode and so the electron heating occurs in a thin skin-depth layer. Such mechanism of the power absorption or deposition is a great advantage to generate plasmas in a limited space without magnetic-field confinement, which would contribute to a simple structure and long-time operation of the system with no electrodes, neutralizers, and magnets. Previously, we carried out a comprehensive numerical and experimental investigation of the microplasma generation, micronozzle flow, and thrust performance with working or propellant gas of argon (Ar).[34] Then, a thrust of > 1 mN was demonstrated with 4.0-GHz microwaves of several W, while the specific impulse remained relatively low (< 100 s), and so the advantage was not sufficient over micro chemical propulsion.

This paper presents a study of the microwave-excited microplasma thruster with hydrogen (H_2) and helium (He) as a propellant. In practice, H_2 and He are often employed for plasma thrusters of electrothermal type because of their light masses, which give a high specific impulse in conventional large-scale propulsion systems.[39–41] However, there have been few studies of the micropropulsion system with such light-mass propellants, because their high diffusivity and thermal conductivity might lead to significant thermal energy losses and so to no improvement of the thrust performance. Sec. II describes the numerical model and results for the microplasma generation and micronozzle flow with working gas of He. The model is concerned with the entire region through the microplasma source to micronozzle, to analyze the electromagnetic wave propagation, plasma evolution, gas/plasma flow evolution (from subsonic to supersonic), and thrust performance. Then, Sec. III gives the experimental setup and results with H_2 as well as He, where the plasma density and gas temperature were measured in the plasma source region by optical emission spectroscopy, along with the thrust performance (thrust and specific impulse). A comparison between the numerical and experimental results is made for He, and a difference in microplasma generation, micronozzle flow, and thrust performance is discussed between light (H_2, He) and heavy (Ar) propellant gases. Finally, Sec. IV summarizes conclusions of this paper.

II. NUMERICAL ANALYSIS

A. Model

The numerical model presently employed has been detailed in our previous paper.[34] Briefly, the model consisted of an electromagnetic module (EM) for microwave propagation in interacting with plasmas and a fluid module (FM) for plasma flows with two (electron and heavy particle) temperatures. The former employed the finite difference time-domain (FDTD) approximation, being applied to the microplasma source region, to analyze the microwave power absorbed in the plasma. The latter employed two-temperature fluid equations, being applied to the entire region through the microplasma source to micronozzle (or through subsonic to supersonic), to analyze the plasma and nozzle flow characteristics. Gas-phase reaction processes were taken into account in both regions along with plasma-wall interactions in a limited space, and the analysis of the nozzle flow finally gave the thrust performance achieved. The numerical analysis relied on the azimuthally symmetric coordinate system [two-dimensional (2D) $r-z$ system, $\partial/\partial\theta = 0$] assuming that: (i) the plasma is a two-phase medium consisting of electrons and heavy particles (ions and neutrals), and the temperature of electrons is different from that of heavy particles [$T_e \neq T_h\,(= T_i = T_n)$]. (ii) The plasma is macroscopically quasi-neutral, or the electron density equals that of ions ($n_e = n_i$). (iii) The atomic processes in the gas phase are electron-impact excitation/de-excitation and ionization/recombination, taking into account metastables as well as ground-state atoms (neutral density $n_n = n_g + n_*$ with ground-state n_g and metastable n_* ones). (iv) The charged particles (ions and electrons) diffuse toward the walls according to the ambipolar diffusion. (v) The sheath structures are neglected at the plasma-wall interfaces. (vi) The gas/plasma flow is laminar, and the convective velocity $\mathbf{v}$ is the same for all species (electrons and heavy particles). (vii) In the microplasma source, moreover, the microwave energy is absorbed by plasma electrons, which in turn, transferred to heavy particles through elastic collisions between them.

The EM module for the microplasma source consisted of Maxwell's equations for electromagnetic fields of microwaves and equations for plasma electrons (neglecting the Lorentz force and pressure gradient). Assuming the azimuthal symmetry of the configuration, only the transverse magnetic waves were taken to exist in the plasma chamber with the electric $\mathbf{E} = (E_r, 0, E_z)$ and magnetic $\mathbf{B} = (0, B_\theta, 0)$ fields of microwaves. The transverse electromagnetic waves were injected into the system at the excitation plane (1.2 mm upstream of the end of the coaxial cable), and the total power injected thereat was monitored as

$$P_{\text{in}} = \frac{1}{\mu_0}\int_A (\mathbf{E}\times\mathbf{B})dA,$$

TABLE I. Inelastic electron collision processes used in the simulation (H_j is the excitation/de-excitation energy of the reaction j).

j	Process	Reaction	H_j (eV)	Ref.
R1	Ground state ionization	$He + e \rightarrow He^+ + 2e$	24.6	48–50
R2	Ground state excitation	$He + e \rightarrow He^* + e$	19.8	48–50
R3	Step-wise ionization	$He^* + e \rightarrow He^+ + 2e$	4.8	51–53
R4	Three-body recombination	$He^+ + 2e \rightarrow He + e$	−24.6	—
R5	Superelastic collision	$He^* + e \rightarrow He + e$	−19.8	—
R6	Two-body recombination	$He^+ + e \rightarrow He^* + (h\nu)$	−4.8	—

where μ_0 is the magnetic permeability of the vacuum and A is the cross section concerned. The boundary conditions for the EM equations were the same as those in Ref. 34, including Mur's first-order absorbing boundary condition applied to the field component E_r at the left end of the coaxial cable (0.8 mm further upstream of the excitation plane). In addition, the total absorbed power in the plasma was calculated as

$$P_{\text{abs}} = \int_V Q_{\text{abs}} dV = \int_V \left(\frac{1}{t_p} \int_{t_p} \mathbf{j} \cdot \mathbf{E} dt \right) dV,$$

assuming that the power absorption $\mathbf{j} \cdot \mathbf{E}$ in the plasma arises only from the classical Ohmic heating of electrons, where $\mathbf{j}$ is the plasma or electron current density induced by microwaves, t_p the period of the electromagnetic waves, and Q_{abs} the time-averaged power density absorbed. The spatially averaged power density absorbed per unit volume was given by $\bar{Q}_{\text{abs}} = P_{\text{abs}}/V$ with the plasma volume V.

The FM module for the microplasma source and micronozzle consisted of two-temperature Navier-Stokes equations and the equation of state for a two-phase medium consisting of electrons and heavy particles (ions and neutrals): the overall mass continuity, overall momentum conservation, conservation of electrons,[42] conservation of metastables, energy conservation of electrons, energy conservation of heavy particles, and equation of state. In the FM equations, the transport coefficients were taken from Refs. 43–45 including the viscosity η, ambipolar diffusion coefficient D_a, diffusivity D_* of metastable He* in He, and thermal conductivity κ_s for electrons ($s = e$) and heavy particles ($s = h$). The energy exchange term due to elastic collisions between electrons and heavy particles was taken from Refs. 46 and 47. Moreover, the electron-impact excitation/de-excitation and ionization/recombination processes were taken into account as listed in Table I. In the terms concerned with inelastic electron collision processes, the ionization and excitation rates (for reactions R1–R3) were taken from Refs. 48–53, and the rate coefficients for the reverse processes (R4–R6) were determined from the so-called principle of detailed balance. The rate coefficients for elastic momentum-transfer and forward reactions (R1–R3) in He are shown in Fig. 2 as a function of electron temperature T_e, together with those in Ar. It is noted here that the rate coefficient for electron impact ionization of metastable He* atoms (R3) appears to be large in Refs. 48–50, in view of the cross section for electron impact ionization of metastable He* and Ar* atoms in Refs. 51–53;

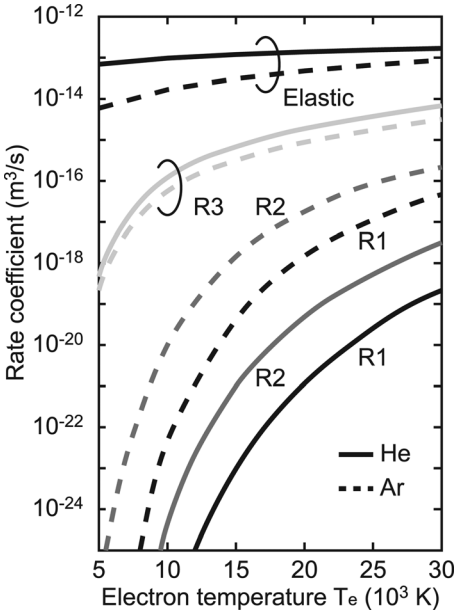

FIG. 2. Rate coefficients for elastic and inelastic electron collision processes in He (solid lines, see Table I) as a function of electron temperature T_e, together with those in Ar (dashed lines).

thus, we took the rate coefficient for metastable ionization (R3) in He that is five times smaller than that previously given in Refs. 48–50. The ionization (R1) and excitation (R2) rate coefficients for He are two–three orders of magnitude smaller than those for Ar, while the elastic momentum-transfer rate coefficient is larger than that for Ar. These differences would lead to a significantly lower plasma and metastable densities in He plasma, compared with those in Ar plasma, while the plasma electron temperature would remain almost unchanged. The transport coefficients are also shown in Fig. 3 as a function of gas or heavy particle temperature T_h and electron temperature T_e (see Ref. 34 for the source of the data on Ar in Figs. 2 and 3). The thermal conductivity and diffusion coefficient for He are ∼ ten times higher than those for Ar, while the viscosity for He is relatively similar to that for Ar. Thus, the thermal loss and the loss of plasma particles (ions, electrons, and metastables) to chamber walls are expected to be more significant in He plasma, while the viscous dissipation in boundary layers is expected to remain relatively unchanged. The boundary conditions for the FM equations were the same as those in Ref. 34: the heavy particle temperature T_h at the interfaces was assumed to be isothermal with a wall temperature $T_w = 500$ K in the plasma source region (as will be validated later in Sec. III A, Experimental setup), and the radiative wall condition was employed for T_h in the nozzle region.

The numerical procedures have also been detailed in our previous paper.[34] The EM equations for the microplasma source were solved by using the FDTD approximation. The FM equations for the microplasma source and micronozzle were all discretized in a finite difference manner, and the discrete equations were solved by using an implicit lower-upper symmetric Gauss-Seidel scheme (LU-SGS).[54] A self-consistent solution was obtained by applying the different timescale integration to the two modules of EM and FM,

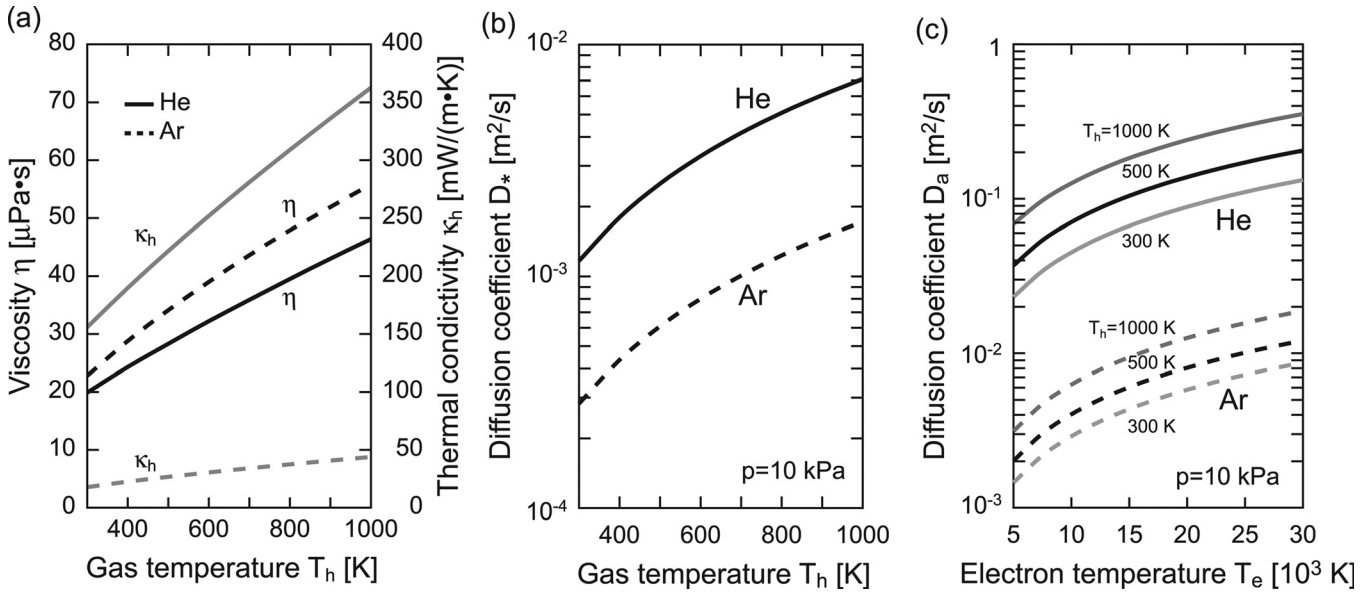

FIG. 3. Transport coefficients for He (solid lines) as a function of (a), (b) gas or heavy particle temperature T_h, and (c) electron temperature T_e, together with those for Ar (dashed lines): (a) viscosity η and thermal conductivity κ_h, (b) diffusion coefficient D_* for metastables, and (c) ambipolar diffusion coefficient D_a for ions and electrons, where $p = n_g k_B T_h$ denotes the gas pressure.

where the procedures were repeated until the plasma and fluid properties converged in the entire region of plasma source and nozzle to finally also give the thrust performance.

B. Numerical results

Figures 4(a)–4(h) show the spatial distribution of the electron density n_e, electron temperature T_e, heavy particle temperature T_h, absorbed power density $Q_{\rm abs}$, pressure p, axial flow velocity u, He gas or ground-state density n_g, and He* metastable-state density n_* in the microplasma source, respectively, calculated for an input power $P_{\rm in} = 6.0$ W of $f = 4$ GHz microwaves, He mass flow rate $\dot{m} = 0.15$ mg/s (flow rate of 50 sccm), and quartz chamber and envelope (relative permittivity $\varepsilon_r = \varepsilon_d = 3.8$). Here, the pressure is given by $p = p_e + p_h = n_e k_B T_e + n_h k_B T_h = n_e k_B (T_e + T_h) + n_n k_B T_h \approx n_g k_B T_h$ with the Boltzmann constant k_B, and the mass density is given by $\rho = m_e n_e + m_h n_h \approx m_h n_h \approx m_h n_g$ with the mass $m_h\,(= m_i = m_n)$ and density $n_h\,(= n_i + n_n = n_e + n_n)$ of heavy particles. The absorbed power calculated in the plasma is $P_{\rm abs} = 4.5$ W/m in total, corresponding to the average power density $\bar{Q}_{\rm abs} = 5.7 \times 10^8$ W/m^3. The plasma electron density n_e and temperature T_e exhibit their maxima near the end of the dielectric envelope of the antenna ($n_e \approx 1.8 \times 10^{19}$ m^{-3}, $T_e \approx 2.0 \times 10^4$ K), which is consistent with the distribution of the absorbed power density $Q_{\rm abs}$. On the other hand, the heavy particle temperature T_h exhibits its maximum in a space between the end of the dielectric envelope and the end wall of the dielectric plasma source chamber ($T_h \approx 650$ K), where the micronozzle is located to achieve the aerodynamic acceleration of high temperature plasmas through supersonic expansion into vacuum. In addition, the pressure calculated is almost uniform in the plasma source ($p \approx 10$ kPa), and the flow velocity is increased in the axial direction toward the end of the source region (up to $u \approx 60$ m/s).

A comparison with numerical results for Ar (Ref. 34) indicates that the electron n_e and metastable n_* densities in He plasma are one–two orders of magnitude lower than those in Ar plasma, because of smaller ionization and excitation rate coefficients and larger diffusion coefficients for He. The electron temperature T_e and absorbed power density $Q_{\rm abs}$ are locally a little higher in He than in Ar plasmas; however, in contrast to Ar, T_e in He is substantially decreased towards the end of the source chamber or the nozzle inlet, owing to more significant energy loss due to elastic and inelastic collisions between electrons and heavy particles in He. The heavy particle temperature T_h in He plasma is only a little lower than that in Ar plasma ($T_h \approx 890$ K in Ar)[34]; this is attributed primarily to a more significant thermal energy gain due to elastic collisions between electrons and heavy particles in He as compared to that in Ar, which tends to offset a more significant thermal energy loss due to the higher thermal conductivity in He. Moreover, the flow velocity u in He plasma is two–five times larger than that in Ar plasma, and correspondingly, the pressure p and gas density n_g are significantly lower in He than in Ar, because u in the plasma source region is governed by the choking ($Ma = u/a = 1$) at the nozzle throat; in effect, the sonic speed $a = (\gamma k_B T_h / m_h)^{1/2}$ of He is higher than that of Ar, where $\gamma = 5/3$ denotes the specific heat ratio for monoatomic gases.

Also shown in Figs. 4(i) and 4(j) are snapshots of the distribution of the radial E_r and axial E_z electric fields of microwaves. The corresponding extended views of the electric fields in the dielectric as well as in the plasma are also shown in Figs. 5(a) and 5(b). These results are similar in part to those for Ar,[34] indicating that the strength of E_r is more than ten times smaller than that of E_z in the plasma, while the former is about ten times larger than the latter in the dielectric. Moreover, the peak position of the absorbed power density $Q_{\rm abs}$ in the plasma corresponds to that of E_z

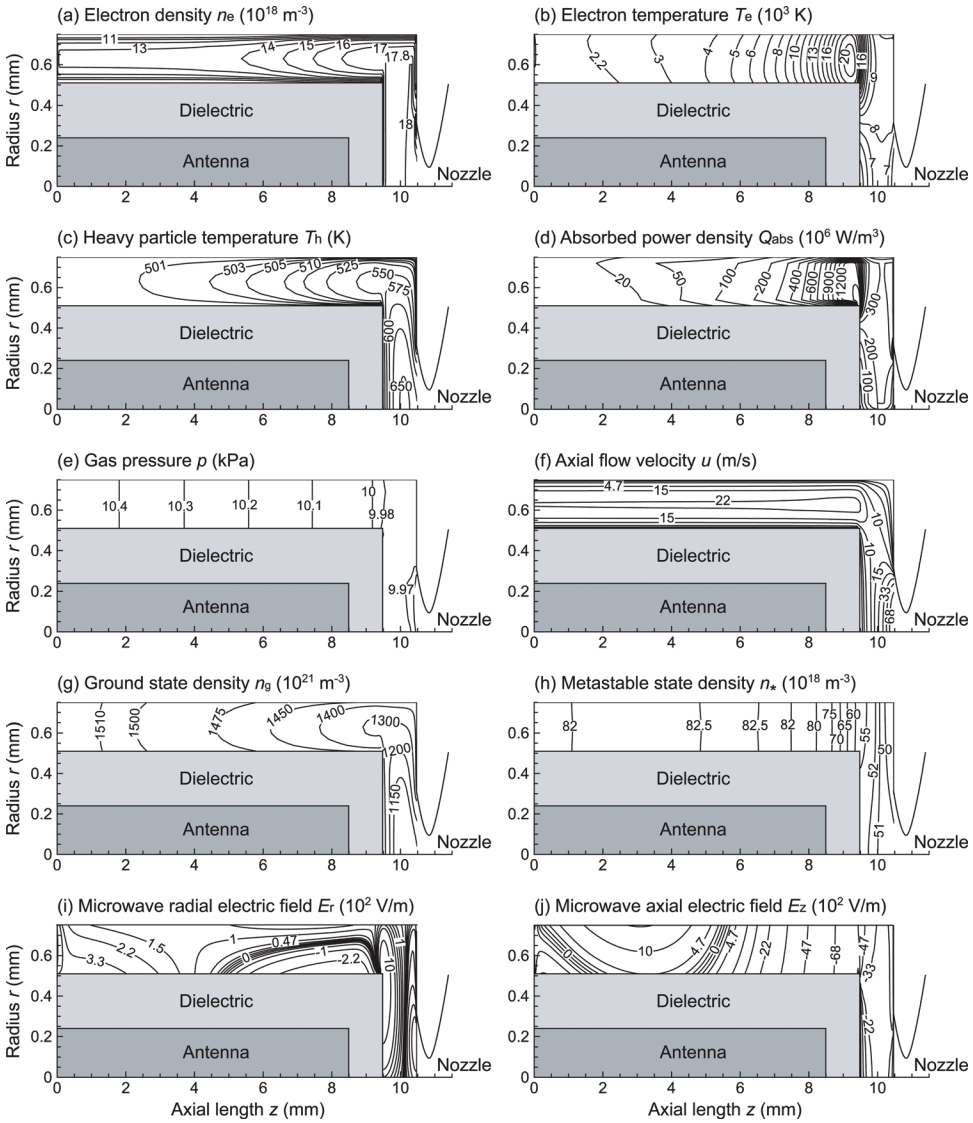

FIG. 4. (Color online) Distribution of the (a) electron density n_e, (b) electron temperature T_e, (c) heavy particle temperature T_h, (d) absorbed power density Q_{abs}, (e) gas pressure p, (f) axial flow velocity u, (g) He gas or ground-state density n_g ($\rho \approx m_h n_g$), and (h) He* metastable-state density n_* in the microplasma source, calculated for an input power $P_{in} = 6.0$ W of $f = 4$ GHz microwaves, He mass flow rate $\dot{m} = 0.15$ mg/s (flow rate of 50 sccm), and quartz chamber and envelope ($\varepsilon_d = 3.8$). Here, the diameter and length of the antenna are $d_{an} = 0.48$ mm and $L_{an} = 8.5$ mm, respectively. The inner diameter, outer diameter, and length of the dielectric envelope covering the antenna are $d_{d,in} = d_{an} = 0.48$ mm, $d_{d,out} = 1.02$ mm, and $L_d = 9.5$ mm, respectively. The inner diameter, outer diameter, and length of the dielectric chamber of the microplasma source are $d_{s,in} = 1.44$ mm, $d_{s,out} = 3.0$ mm, and $L_s = 10.5$ mm, respectively. The microwave power absorbed in the plasma was calculated as $P_{abs} = 4.5$ W. Also shown is a snapshot of the distribution of the (i) radial E_r and (j) axial E_z electric fields of microwaves in the microplasma region.

(not E_r), implying that the axial E_z is the major component of microwave electric fields that contributes to Q_{abs} and thus to P_{abs}. The present numerical analysis gives a high absorption efficiency $P_{abs}/P_{in} \approx 75$ % in He (>80% in Ar),[34] which is ascribed to the localized absorption of microwaves or inhomogeneous heating of electrons in the interaction of electromagnetic waves with nonuniform plasmas. However, it should be noted here that the present results for He show no significant characteristic of surface wave-excited plasmas as can be seen in the case of Ar,[34] where the strength E_z in the plasma is largest near the plasma-dielectric interfaces, further increasing with increasing axial distance downstream toward the end of the antenna or dielectric envelope. This is attributed to the lower plasma electron densities n_e in He, which do not satisfy in part the conditions for surface waves;[55] in practice, the surface wave is assumed to propagate in a thin skin depth layer of thickness $\delta = c/\omega_{pe}$ along the plasma-dielectric interfaces for densities $n_e > n_{cr}$. Here, c denotes the speed of light in vacuum, $\omega_{pe} = (n_e e^2/m_e \varepsilon_0)^{1/2}$ the plasma electron frequency, $n_{cr} = (1 + \varepsilon_d) n_c$ the critical density for surface waves, and $n_c = \varepsilon_0 m_e \omega^2/e^2$ the cutoff density for electromagnetic waves of frequency $f = \omega/2\pi$; moreover, e is the magnitude of electron charge, m_e the mass of electron, and ε_0 the electric permittivity of vacuum. In the case of He with typically $n_e = 2 \times 10^{19}$ m^{-3} ($n_e = 2 \times 10^{20}$ m^{-3} in Ar),[34] the frequency $f = 4$ GHz and dielectric constant $\varepsilon_d = 3.8$ give $n_{cr} = 9.1 \times 10^{17}$ m^{-3} and $\delta = 1.2$ mm ($\delta = 0.38$ mm in Ar); thus, in He, $\delta > R_c$ while $n_e > n_{cr}$, where $R_c = (d_{d,out} - d_{d,in})/2 = 0.24$ mm is the characteristic radial length of the plasma presently concerned.

Figures 6(a)–6(h) show the distribution of the electron density n_e, electron temperature T_e, heavy particle temperature T_h, Mach number $Ma = |\mathbf{v}|/a$, pressure p, axial flow velocity u, He gas or ground-state density n_g, and He* metastable-state density n_* in the micronozzle, respectively, obtained in the same numerical simulation as Figs. 4 and 5. The temperature T_h, Mach number Ma, pressure p, flow velocity u, and gas n_g and metastable n_* densities exhibit a characteristic of the subsonic-supersonic flow or aerodynamic acceleration of flow in the converging-diverging nozzle: Ma and u increase with increasing axial distance, with $Ma = 1$

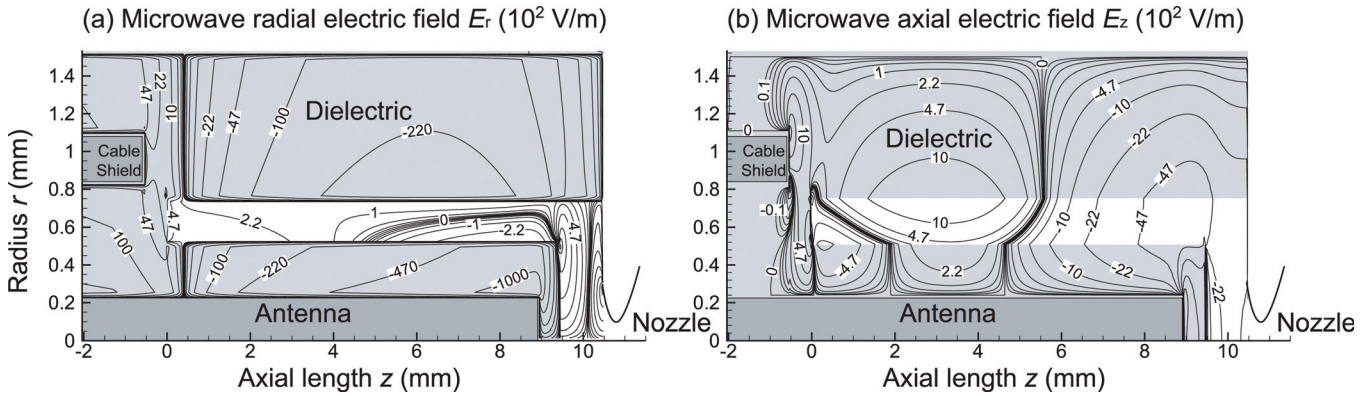

FIG. 5. (Color online) Extended view of a snapshot of the distribution of the (a) radial E_r and (b) axial E_z electric fields of microwaves in the microplasma source, corresponding to Figs. 4(i) and 4(j). The figure includes the region of coaxial cable for microwave injection and the region of dielectric materials containing the plasma. Note that the excitation plane for microwave injection in the numerical analysis is at $z = -1.2$ mm, and the boundary for Mur's first-order absorbing condition is at $z = -2$ mm.

being at around the throat, while T_h, p, n_g, and n_* decrease downstream along the nozzle axis. However, the contour of T_h, Ma, and u indicates that the boundary layer associated with viscosity is relatively thick in the micro-nozzle, especially in the divergent or supersonic portion of the nozzle.[56] In practice, the flow velocity u is lower and the temperature T_h is higher closer to the nozzle walls in the diverging portion; moreover, the flow therein is supersonic ($Ma > 1$) around the nozzle axis, while subsonic ($Ma < 1$) near the walls over roughly half of the nozzle cross section. Note that the decrease of the temperature T_h along the nozzle axis is not so significant as compared to the change of Ma, p, u, n_g, and n_*, owing to heating due to viscous dissipation in thick boundary layers. It is further noted that the plasma density n_e decreases downstream along the nozzle axis, which is similar to the behavior of the pressure p and gas n_g and metastable n_* densities; on the other hand, the electron temperature T_e exhibits a substantial decrease along the axis, which is more significant as compared to the behavior of the temperature T_h.

A comparison with numerical results for Ar (Ref. 34) indicates that the flow velocity u in the nozzle is more than two times larger in He than that in Ar, owing to the higher sonic speed of He, although the aerodynamic acceleration of the flow in He is not so strong as compared to that in Ar, owing to lower pressures p or gas densities n_g in the plasma source region in He. Moreover, the decrease of the electron

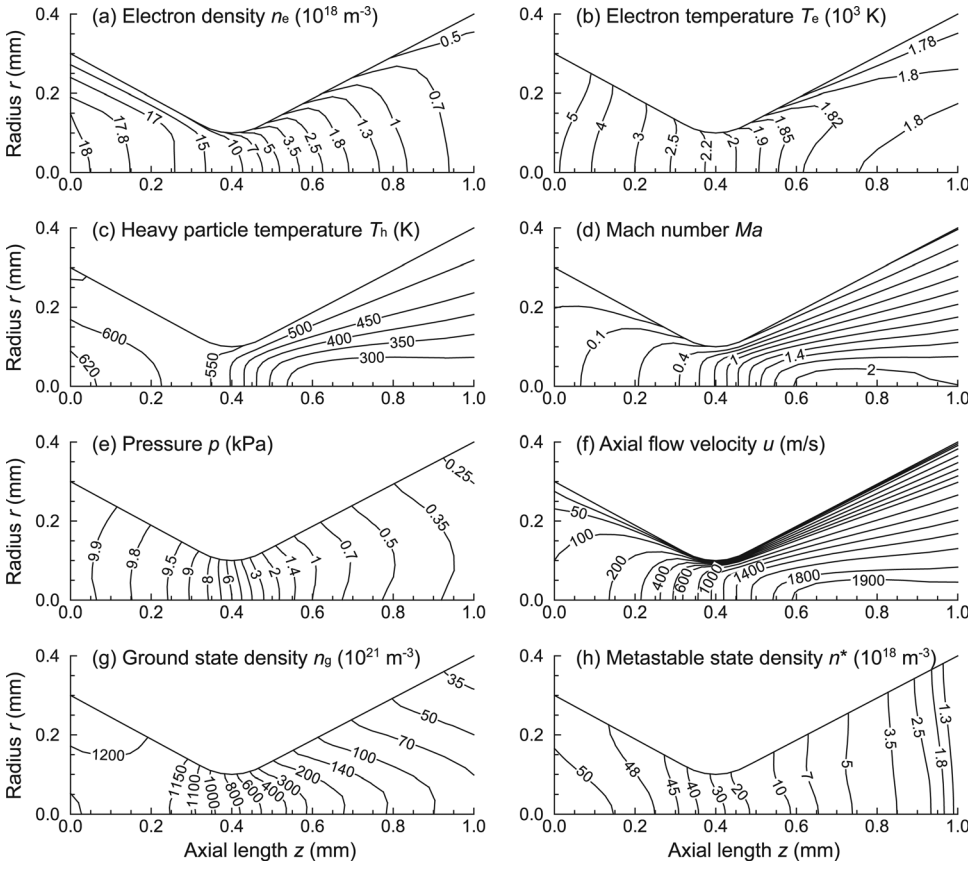

FIG. 6. Distribution of the (a) electron density n_e, (b) electron temperature T_e, (c) heavy particle temperature T_h, (d) Mach number Ma, (e) pressure p, (f) axial flow velocity u, (g) He gas or ground-state density n_g ($\rho \approx m_h n_g$), and (h) He* metastable-state density n_* in the micronozzle, obtained in the same numerical simulation as Figs. 4 and 5. The nozzle shown has an inlet, throat, and exit diameter of $d_{in} = 0.6$ mm, $d_{th} = 0.2$ mm, and $d_{ex} = 0.8$ mm, respectively, with a diverging angle of $\theta = 26.6°$ and a total length of 1 mm.

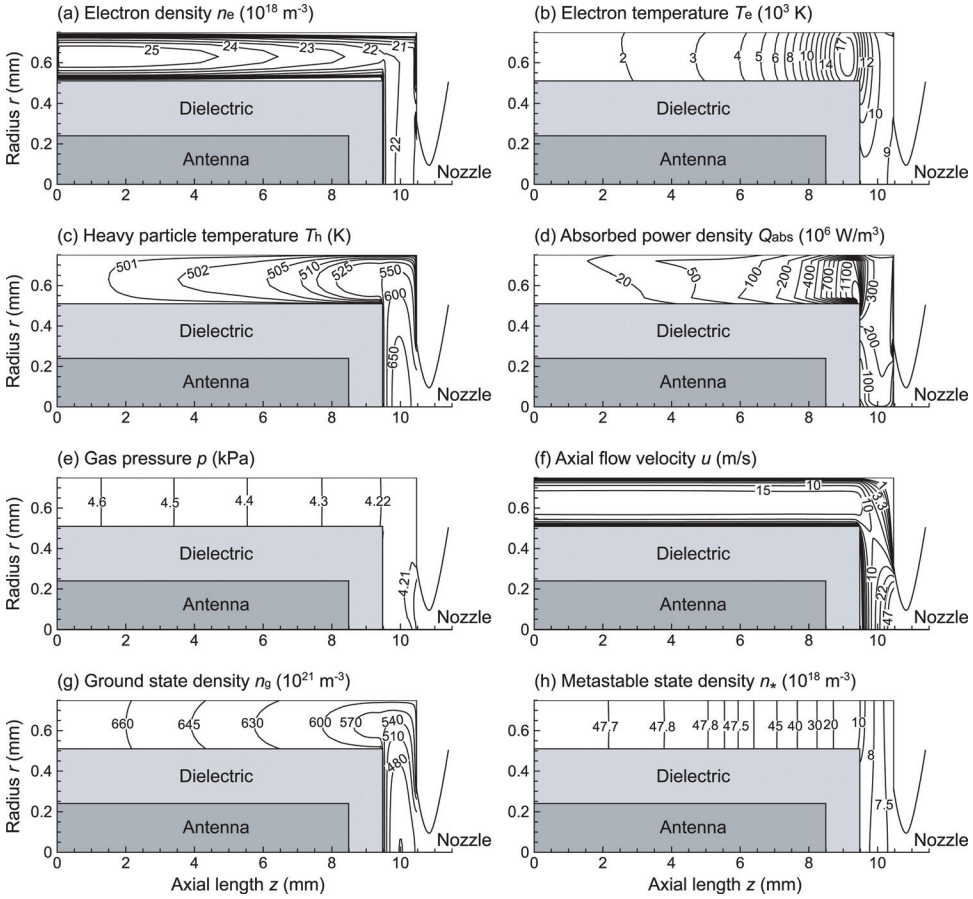

FIG. 7. (Color online) Distribution of the (a) electron density n_e, (b) electron temperature T_e, (c) heavy particle temperature T_h, (d) absorbed power density Q_{abs}, (e) gas pressure p, (f) axial flow velocity u, (g) He gas or ground-state density n_g ($\rho \approx m_h n_g$), and (h) He* metastable-state density n_* in the microplasma source for a He mass flow rate $\dot{m} = 0.059$ mg/s (or a flow rate of 20 sccm), calculated with the other parameters being the same as Figs. 4–6. The microwave power absorbed in the plasma was calculated as $P_{abs} = 4.4$ W.

temperature T_e downstream along the nozzle axis in He is significantly large as compared to that in Ar, primarily because of more significant energy loss due to elastic and inelastic collisions between electrons and heavy particles in He.

Figures 7 and 8 show the contour of plasma and flow properties in the microplasma source and micronozzle, respectively, for a reduced He mass flow rate of $\dot{m} = 0.059$ mg/s (flow rate of 20 sccm), calculated with the other parameters being the same as in Figs. 4–6. A comparison between Figs. 4 and 7 indicates that in the plasma source region, reducing the flow rate leads to a decrease in pressure p, flow velocity u, and gas n_g and metastable n_* densities, while the electron density n_e, temperature T_e, heavy particle temperature T_h, and absorbed power density Q_{abs} remain almost unchanged. A comparison between Figs. 6 and 8 indicates that at reduced flow rates, the aerodynamic acceleration of the flow in the nozzle is significantly reduced owing to lower pressures p or gas densities n_g in the plasma source region. These effects of reducing the flow rate are more significant for He, as can be seen from a comparison with numerical results for Ar,[34] because the sonic speed of He is much higher than that of Ar. In practice, the micronozzle flow of He in Fig. 8 remains almost subsonic, or the Mach number is $Ma < 1$, over almost the entire region of the nozzle, where a transition from subsonic to supersonic flow on axis occurs a little downstream of the throat (not at the nozzle throat) with the minimum T_h and the maximum Ma and u being inside the nozzle (not at the nozzle exit). Thus, it follows that viscous boundary layers next to the nozzle walls[56] impede the flow expansion in the micronozzle more significantly at reduced flow rates in He, where the nozzle flow is heavily underexpanded to decelerate the supersonic flow downstream along the axis in the diverging portion of the nozzle.

III. EXPERIMENT

A. Experimental setup

The experimental setup has been detailed in our previous paper.[34] The microplasma source chamber was made of a quartz tube ($\varepsilon_d = 3.8$) $L_s = 10.5$ mm long, $d_{s,in} = 1.5$ mm in inner diameter, and $d_{s,out} = 3.0$ mm in outer diameter, which was similar to the configuration of the microplasma source shown in Figs. 4, 5 and 7. The center conductor of a semi-rigid coaxial cable, protruding 10 mm beyond the insulator and outer conductor, was covered with a dielectric envelope, which was then inserted in the source chamber as a microwave antenna $L_{an} = 8.5$ mm long and $d_{an} = 0.5$ mm in diameter. The dielectric envelope of quartz ($\varepsilon_d = 3.8$) covering the antenna was $L_d = 9.5$ mm long, $d_{d,in} = 0.5$ mm in inner diameter, and $d_{d,out} = 1.0$ mm in outer diameter. The plasma source chamber and antenna were inserted into a stainless-steel housing to cover the microplasma source with a metal grounded, where an annular spacing was retained for feeding the propellant gas. The microplasma source thus

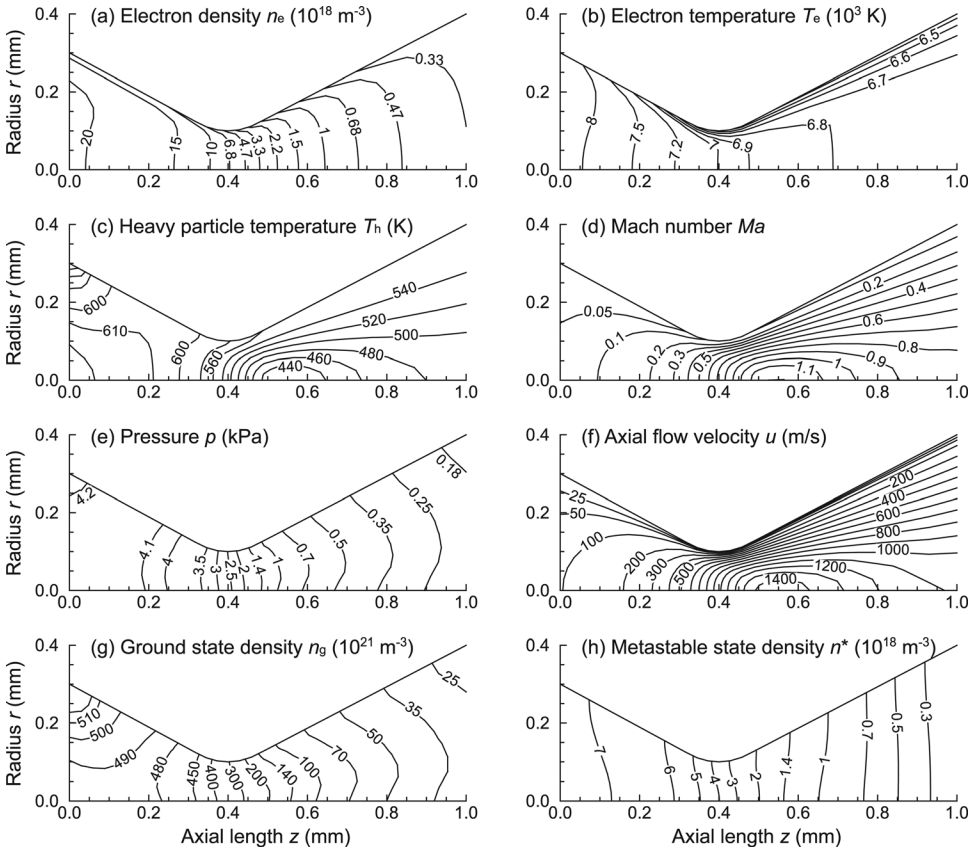

FIG. 8. Distribution of the (a) electron density n_e, (b) electron temperature T_e, (c) heavy particle temperature T_h, (d) Mach number Ma, (e) pressure p, (f) axial flow velocity u, (g) He gas or ground-state density n_g ($\rho \approx m_h n_g$), and (h) He* metastable-state density n_* in the micronozzle, obtained in the same numerical simulation as Fig. 7.

configured was located in a vacuum chamber pumped down by a dry and turbomolecular pump.

Microwave signals of $f = 4$ GHz from a signal generator were amplified through a four-stage semiconductor amplifier to powers of nominally $P_{\text{in}} \leq 6$ W, and then fed into the microplasma source through the semi-rigid coaxial cable, where a miniature three-stub tuner was used to suppress the reflection of microwaves. The propellant or working gas was He and H_2 in this study, being supplied through a mass flow controller; in some cases, a small amount ($< 1\%$) of N_2 and H_2 was added for plasma diagnostics. The gas pressure p_0 ($= p \approx n_g k_B T_h$) in the microplasma source was measured by a pressure gauge set upstream of the source chamber. The micronozzle of converging-diverging type was fabricated in a 1-mm-thick quartz plate, having an inlet, throat, and exit diameter of $d_{\text{in}} = 0.6$, $d_{\text{th}} = 0.2$, and $d_{\text{ex}} = 0.8$ mm, respectively, which was similar to the nozzle configuration shown in Figs. 6 and 8; the micronozzle was attached to the end of the microplasma source chamber. It is noted here that the gas flow rate (or mass flow rate $\dot{m}$) and the source pressure p_0 measured with and without plasma discharge were approximately related by the quasi-one-dimensional nozzle flow equation for an isentropic flow of perfect gas,[34,56–58] assuming the source temperature T_0 ($\approx T_h$) to be the room temperature in cold gas operation and to be the gas temperature spectroscopically measured in plasma discharge operation. At He gas flow rates of 2–70 sccm, the source pressure was in the range $p_0 = 0.5-12$ kPa with plasma discharge at $P_{\text{in}} = 6$ W, and in the range $p_0 = 0.2-7$ kPa without plasma discharge. It is further noted that by using a radiation thermometer and temperature labels, the wall temperature of the microplasma source chamber was estimated to be typically $T_w \approx 500$ K with the plasma discharge on at $P_{\text{in}} = 6$ W, which was only a little lower than the melting point of Viton® O-rings set in the present microplasma chamber system.

To characterize the microplasma concerned, the optical emission from the plasma was observed in the side-view direction through a 1-mm-diam small hole of the stainless-steel housing at around the end of the antenna or dielectric envelope (just upstream of the micronozzle inlet).[34] A 50-cm focal length spectrograph/monochromator was employed in these experiments, with a grating of 2400 lines/mm and charge-coupled device (CCD) detector, where a set of lenses were used to collect the emission from the plasma and focus it on the entrance slit of the spectrometer. The spectral resolution, determined using a low-pressure Ar discharge lamp, was 0.025 nm with an entrance slit width of 5 μm.

B. Plasma characteristics

The analysis of optical emissions from the plasma has been detailed in our previous paper.[34] The plasma electron density was measured by analyzing the Stark broadening of the H Balmer-β (H_β) spectral line at 486.1 nm, where a small amount ($< 1\%$) of H_2 was added in the case of He. The H_β line broadening is generally appreciated to consist of the instrumentation $\Delta\lambda_{\text{instrum}}$, Doppler $\Delta\lambda_{\text{Doppler}}$ (depending on gas temperature T_g), pressure $\Delta\lambda_{\text{pressure}}$ (depending on T_g and p_0 or gas density n_g), and Stark $\Delta\lambda_{\text{Stark}}$ broadening

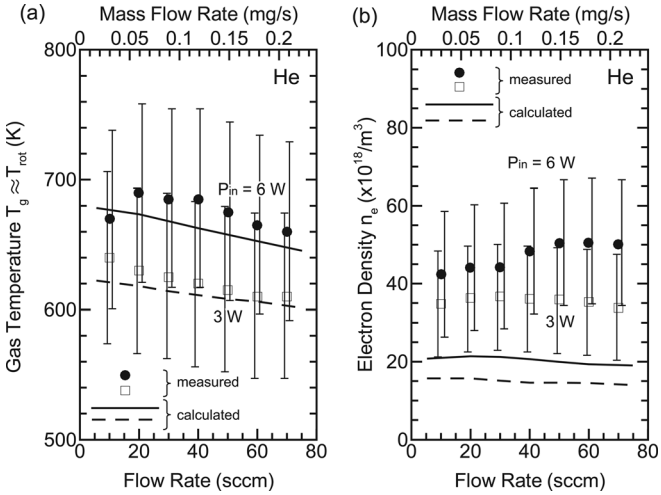

FIG. 9. (a) Plasma electron density n_e and (b) gas temperature $T_g \approx T_{rot}$ measured as a function of He gas flow rate for different microwave powers P_{in}, where changing the flow rate led to a change in pressure p_0 in the microplasma source. These data were taken under the conditions of $f = 4$ GHz and $\varepsilon_d \approx 3.8$, with a small amount (0.05 sccm) of additive gases of N_2 in (a) and H_2 in (b). Also shown in the figure are the curves of n_e and T_g $(= T_h)$ numerically simulated as in Figs. 4 and 7, where the data are those line-averaged in the radial direction between the end of the antenna or dielectric envelope and the inlet of the micronozzle.

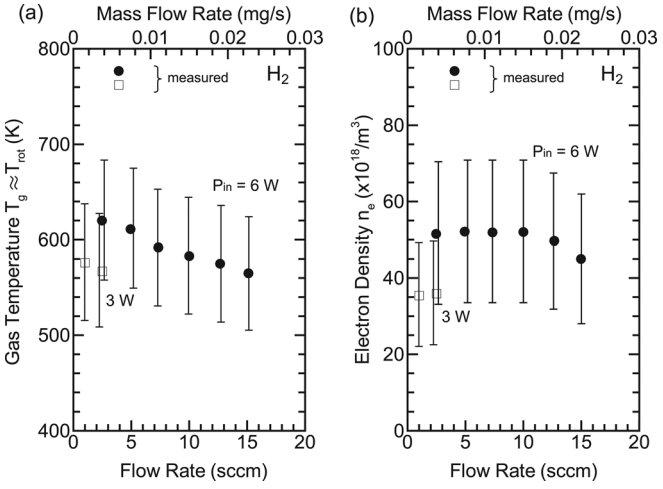

FIG. 10. (a) Plasma electron density n_e and (b) gas temperature $T_g \approx T_{rot}$ measured as a function of H_2 gas flow rate for different microwave powers P_{in}, where changing the flow rate led to a change in pressure p_0 in the microplasma source. These data were taken under conditions of $f = 4$ GHz and $\varepsilon_d \approx 3.8$, with a small amount (0.05 sccm) of additive gas of N_2 in (a).

(depending on n_e and T_e)[34,59–61]; the former two are given by the Gaussian profile and the latter two by the Lorenzian profile, which are then approximated by the Voigt function in total with a full width at half maximum (FWHM) of $\Delta\lambda_V$ (typically, $\Delta\lambda_V \approx 0.05-0.06$ nm in the present experiments). The accuracy of the electron density determined from the Stark broadening relies on the spectral resolution of the measurement system and also on the assumption of analysis of the spectral line broadening; in practice, the present accuracy was estimated to be about $\pm 20\%$, primarily owing to the resolution $\Delta\lambda_{instrum} \approx 0.025$ nm of the spectrometer system employed. Moreover, the gas/rotational temperature was measured by adding a small amount ($< 1\%$) of N_2 and analyzing the vibronic spectrum of the N_2 2nd positive $(0, 2)$ band at 380.4 nm.

Figures 9 and 10 show the plasma electron density n_e and gas/rotational temperature $T_g \approx T_{rot}$ measured as a function of He and H_2 gas flow rates, respectively, for different microwave input powers P_{in}, where changing the flow rate led to a change in pressure p_0 or gas density n_g in the microplasma source as in Ref. 34. The electron density was in the range $n_e \approx (2-5) \times 10^{19}$ m^{-3}, and the gas temperature was in the range $T_g \approx T_{rot} \approx 600-700$ K in He discharges of Fig. 9, where n_e was about five times lower and T_g was a little lower than those in Ar discharges.[34] The temperature $T_g \approx T_{rot}$ was observed to increase with increasing P_{in} and to slightly decrease with increasing flow rate (or with increasing p_0 or n_g in the plasma source). On the other hand, the density n_e was observed to increase with increasing P_{in} and to remain almost unchanged by varying the flow rate. Also shown in Fig. 9 are the curves of n_e and $T_g (= T_h)$ numerically simulated as in Figs. 4 and 7, indicating that the experiments were in agreement with the numerical analysis, where the numerical data were line-averaged in the radial direction between the end of the microwave antenna or dielectric envelope and the inlet of the nozzle. Similar plasma characteristics were observed in H_2 discharges of Fig. 10, where the discharge could not be established under marginal conditions for sustaining the discharge (at high flow rates of > 15 sccm at $P_{in} = 6$ W and > 2.5 sccm at $P_{in} = 3$ W).

It should be noted that at a constant power input in He and H_2, the gas temperature T_g decreases slightly with increasing gas flow rate (or seems to be almost independent of flow rate), while the electron density n_e is almost independent of flow rate. This implies that more efficient energy transfer from electrons to heavy particles occurs at higher flow rates, which is caused by more frequent elastic collisions between electrons and heavy particles at higher flow rates. In effect, increasing the flow rate leads to an increase in pressure or gas density in the plasma source chamber, as mentioned earlier (in Sec. III A, Experimental setup), which in turn results in more frequent collisions between electrons and heavy particles at higher flow rates. Such cause-and-effect relationships can also be seen through a comparison of T_g and n_e depending on flow rate between He/H_2 and Ar;[34] in the case of Ar, the temperature T_g decreases significantly with increasing flow rate, while the density n_e increases with increasing flow rate. This is attributable to less efficient energy transfer from electrons and heavy particles in Ar, due to lower electron-neutral atom elastic collision rates for Ar (see Fig. 2) and also to smaller electron-to-atom mass ratio m_e/m_h for Ar.

C. Thrust performance

The experimental setup for thrust measurement has been detailed elsewhere,[31] which consisted of a pendulum-type stand for cold-gas operation and a target-type stand for both cold-gas and plasma-discharge operations. In the former, the thruster itself was hung; on the other hand, in the latter, a small concave cylindrical target block was hung downstream

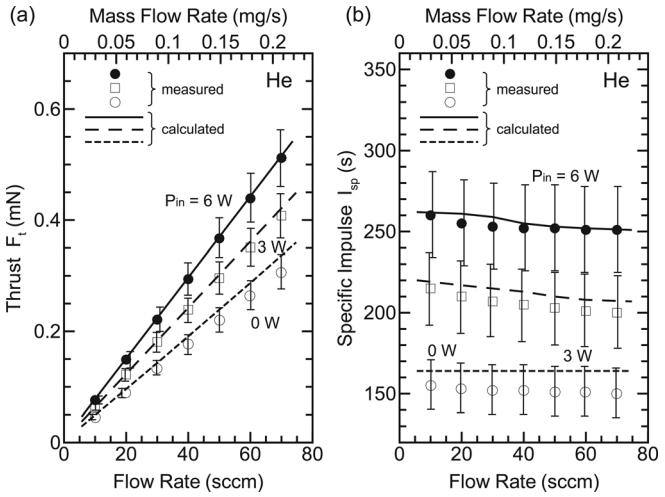

FIG. 11. Thrust performance [(a) thrust F_t and (b) specific impulse I_{sp}] measured as a function of He gas flow rate for different microwave powers P_{in} under the same conditions as in Fig. 9 ($f = 4$ GHz, $\varepsilon_d \approx 3.8$). Here, $P_{in} = 0$ W corresponds to the cold-gas operation without plasma discharge. Also shown in the figure are the curves of F_t and I_{sp} calculated from the numerical analysis as in Figs. 6 and 8.

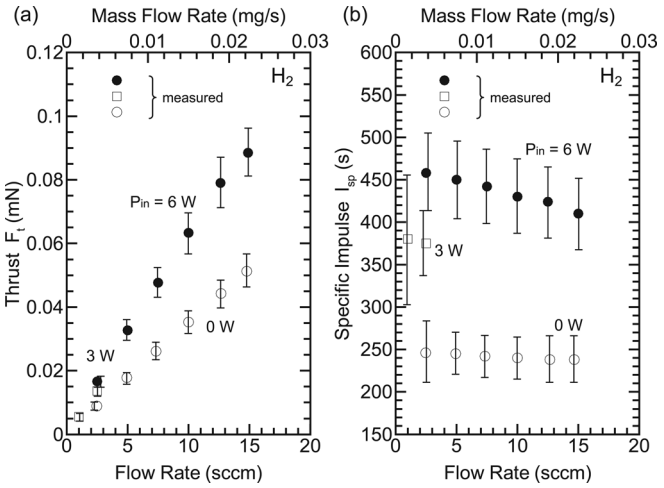

FIG. 12. Thrust performance [(a) thrust F_t and (b) specific impulse I_{sp}] measured as a function of H_2 gas flow rate for different microwave powers P_{in} under the same conditions as in Fig. 10 ($f = 4$ GHz, $\varepsilon_d \approx 3.8$). Here, $P_{in} = 0$ W corresponds to the cold-gas operation without plasma discharge.

of the nozzle exit with the thruster being fixed tightly, and the gas/plasma plume ejected from the thruster struck the target mounted at one end of the pendulum with some weights being at the other end for balance. Here, the target employed was a small Faraday cup-like one made of polytetrafluoroethylene (PTFE), to suppress the effects of reflected particles of the jet plume striking the target. A small displacement of $\Delta X < 0.1$ mm in operation was measured by using a laser displacement gauge having a resolution of $\Delta x < 0.1\,\mu$m. The accuracy of the present thrust measurement was estimated to be about $\pm 10\%$, relying primarily on mechanical issues of the measurement system such as effects of friction of the knife edge on the rotational axis and the reflected jet plume particles on the target.

Figures 11 and 12 show the thrust performance (thrust F_t, specific impulse I_{sp}) measured as a function of He and H_2 gas flow rates, respectively, for different microwave input powers P_{in}, where $P_{in} = 0$ W corresponds to the cold-gas operation without plasma discharge. The measurements showed that the thrust performance was enhanced with the discharge on and with increasing P_{in}; the thrust and specific impulse were typically $F_t \approx 0.51$ mN and $I_{sp} \approx 250$ s, respectively, with the thrust efficiency $\eta_t \approx 10.1\%$ at $P_{in} = 6$ W and a He flow rate of 70 sccm (0.21 mg/s). Also shown in He discharges of Fig. 11 are the curves of F_t and I_{sp} calculated based on the numerical analysis in Sec. II as in Ref. 34, indicating that the experiments were in agreement with the numerical analysis, where the thrust F_t was taken to consist of the momentum and pressure ones, and the temperature T_h was taken to be the room temperature in cold gas operation. It is further noted that the numerical efficiency was in the range $\eta_t \approx 2-12$ % at $P_{in} \approx 3-6$ W and He flow rates of 10–70 sccm. Similar thrust performance was obtained in H_2 discharges of Fig. 12, where the specific impulse I_{sp} was more than 1.5 times higher than that in He, owing to a difference in mass between H_2 and He.[56,58]

Figure 13 shows a summary of the thrust performance (I_{sp} versus F_t) measured for different microwave powers P_{in} and flow rates with three different propellant gases, where the data for He and H_2 were taken from the preceding Figs. 11 and 12, respectively, and the data for Ar were taken from Fig. 14 of our previous paper.[34] It should be noted here that the specific impulse I_{sp} was higher with light-mass He and H_2 than with Ar, while the thrust F_t was larger with Ar than with He and H_2, and that the thrust performance was enhanced with the discharge on and with increasing P_{in} for all these different gases. Thus, it follows that in the microplasma thruster of electrothermal type, the high diffusivity and thermal conductivity of light-mass propellants do not lead to a deterioration of the thrust performance, although the surface-to-volume ratio is high for microplasma sources;

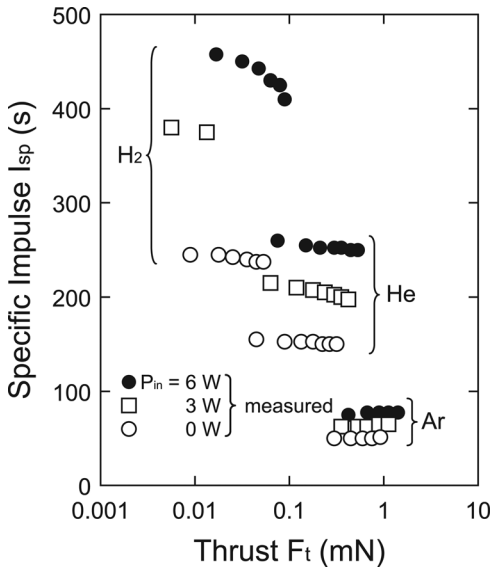

FIG. 13. Thrust F_t versus specific impulse I_{sp} measured for different microwave powers P_{in} and gas flow rates with three different propellant gas. The data for He and H_2 were taken from the preceding Figs. 11 and 12, respectively, and the data for Ar were from Fig. 14 of our previous paper.[34]

in effect, in the present microplasma thruster, the specific impulse I_{sp} was found to be significantly enhanced with light-mass propellants of He and H_2 as compared to that with Ar, as has been known for large-scale propulsion systems.[58] This is attributed primarily to a more significant thermal energy gain due to elastic collisions between electrons and heavy particles in He and H_2 as compared to that in Ar, which tends to offset a more significant thermal energy loss due to the high diffusivity and thermal conductivity of light-mass He and H_2 in the microplasma source of high surface-to-volume ratios.

IV. CONCLUSIONS

Microplasma thruster of electrothermal type has been investigated with feed or propellant gases of He and H_2. The thruster consisted of an azimuthally symmetric microwave-excited microplasma source and a converging-diverging micronozzle. The plasma source was made of a dielectric chamber 1.5 mm in diameter and 10 mm long covered with a metal grounded, having a metal rod antenna on axis covered with a dielectric envelope, which produced high temperature plasmas at around atmospheric pressures. The surface wave-excited plasmas were established by 4.0-GHz microwaves at powers of $P_{in} \leq 6$ W, with the source pressure in the range 0.5–12 kPa at flow rates of 2–70 sccm. The nozzle was also made of a dielectric, being 1 mm long with a throat 0.2 mm in diameter, which converted high thermal energy of plasmas into directional kinetic energy of supersonic plasma flows to obtain the thrust. The microplasma generation, micronozzle flow, and thrust performance with He were numerically analyzed by using a two-dimensional fluid model over the entire region through the microplasma source to the micronozzle, coupled with an electromagnetic model for microwaves interacting with plasmas in the source region. The numerical results indicated that in the micronozzle, viscous boundary layers next to the nozzle walls impede the flow expansion, especially at reduced flow rates, where the supersonic flow is heavily decelerated to subsonic downstream along the axis in the diverging portion of the nozzle.

In experiments, the plasma electron density and gas temperature were measured in the microplasma source at around the top of the microwave antenna, or just upstream of the micronozzle inlet, by optical emission spectroscopy with a small amount of additive gases of H_2 and N_2. In the case of He propellant, the Stark broadening of H Balmer-β line and the vibronic spectrum of N_2 2nd positive $(0,2)$ band indicated that the electron density was in the range $n_e \approx (2-5) \times 10^{19}$ m^{-3} and the gas or rotational temperature was in the range $T_g \approx T_{rot} \approx 600-700$ K. The thrust performance was also measured by using a target-type microthrust stand, giving a thrust in the range $F_t \approx 0.04-0.51$ mN, a specific impulse in the range $I_{sp} \approx 150-270$ s, and a thrust efficiency in the range $\eta_t \approx 2-12$ %. The plasma density, temperature, and thrust performance were enhanced with increasing microwave input power, and the experimental results were consistent with those of numerical analysis depending on microwave power and gas flow rate. Similar plasma characteristics and thrust performance were obtained with H_2 propellant, where the specific impulse I_{sp} of ≤ 450 s was more than 1.5 times higher than that with He, owing to a difference in mass between He and H_2.

A comparison with previous numerical and experimental studies with Ar propellant[34] indicated that the plasma electron density n_e was about three times lower in He and H_2 than in Ar; however, the gas temperature $T_g \approx T_{rot}$ remained a little lower in He and H_2, and the specific impulse I_{sp} in the presence as well as absence of plasma discharge was found to be enhanced by about 3–5 times with light-mass He and H_2, as has been known for large-scale propulsion systems.[58] Moreover, the axial flow velocity u calculated was more than two times larger in He than that in Ar in the microplasma source as well as micronozzle regions owing to the higher sonic speed a of He, because u is governed primarily by the choking $(Ma = u/a = 1)$ at the nozzle throat. Thus, in contrast to general assumptions, it follows that in the microplasma thruster of electrothermal type, the high surface-to-volume ratio of microplasma sources and the high diffusivity and thermal conductivity of light-mass propellants do not lead to a deterioration of the thrust performance. This is attributed primarily to a more significant thermal energy gain due to elastic collisions between electrons and heavy particles in He and H_2 as compared to that in Ar, which tends to offset a more significant thermal energy loss due to the high diffusivity and thermal conductivity of He and H_2 in the microplasma source of high surface-to-volume ratios. It should be concluded that the present microplasma thruster of electrothermal type would be applicable to attitude-control and station-keeping maneuver for microspacecraft in a variety of operation modes, with and without plasma discharge using light- and heavy-mass propellant gases.

ACKNOWLEDGMENTS

This work was supported in part by a Grant-in-Aid for Scientific Research from the Japan Society for the Promotion of Science. The authors would like to thank S. Kitanishi for assistance with experiments.

[1]E. Y. Robinson, H. Helvajian, and S. W. Janson, Aerosp. Am. **Oct.**, 38 (1996).
[2]H. Helvajian and S. W. Janson, in *Microengineering Aerospace Systems*, edited by H. Helvajian (AIAA, Reston, 1999), Chap. II.
[3]J. Mueller, in *Micropropulsion for Small Spacecraft*, edited by M. M. Micci and A. D. Ketsdever (AIAA, Reston, 2000), Chap. III.
[4]J. R. Wilson, Aerosp. Am. **Feb.**, 34 (2003).
[5]M. Tajmar, *Advanced Space Propulsion Systems* (Springer, Vienna, 2004), Chap. 2.
[6]J. Sethian, in *MEMS and Microstructures in Aerospace Applications*, edited by R. Osiander, M. A. G. Darrin, and J. L. Champion (CRC, Boca Raton, 2005), Chap. 11.
[7]H. Horisawa, K. Onodera, T. Noda, and I. Kimura, Vacuum **80**, 1244 (2006).
[8]H. Okamoto and M. Nishida, Trans. Jpn. Soc. Aeronaut. Space Sci. **48**, 187 (2006).
[9]T. Deconinck, S. Mahadevan, and L. L. Raja, IEEE Trans. Plasma Sci. **36**, 1200 (2008).
[10]P. S. Kothnur and L. L. Raja, J. Appl. Phys. **97**, 043305 (2005).
[11]P. S. Kothnur and L. L. Raja, Contrib. Plasma Phys. **47**, 9 (2007).
[12]T. Ito and M. A. Cappelli, Appl. Phys. Lett. **89**, 061501 (2006).
[13]T. Ito, N. Gascon, W. S. Crawford, and M. A. Cappelli, J. Propul. Power **23**, 1068 (2007).

[14]H. Kataharada, Y. Takao, N. Yamamoto, H. Ijiri, and H. Nakashima, Thin Solid Films **506–507**, 605 (2006).
[15]N. Yamamoto, S. Kondo, T. Chikaoka, H. Nakashima, and H. Masui, J. Appl. Phys. **102**, 123304 (2007).
[16]N. Yamamoto, K. Tomita, N. Yamasaki, T. Tsuru, T. Ezaki, Y. Kotani, K. Uchino, and H. Nakashima, Plasma Sources Sci. Technol. **19**, 045009 (2010).
[17]H. Koizumi and H. Kuninaka, J. Propul. Power **26**, 601 (2010).
[18]A. Dunaevsky, Y. Raitses, and N. J. Fisch, Appl. Phys. Lett. **88**, 251502 (2006).
[19]M. Tajmar, A. Genovese, and W. Steiger, J. Propul. Power **20**, 211 (2004).
[20]S. Castro and R. Bocanegra, Appl. Phys. Lett. **88**, 123105 (2006).
[21]J. Schein, N. Qi, R. Binder, M. Krishnan, J. K. Ziemer, J. E. Polk, and A. Anders, Rev. Sci. Instrum. **73**, 925 (2002).
[22]T. Moeller and Y. K. Chang, Aerosp. Sci. Technol. **11**, 481 (2007).
[23]M. Keidar, I. D. Boyd, J. Luke, and C. Phipps, J. Appl. Phys. **96**, 49 (2004).
[24]J. Aoyagi, M. Mukai, Y. Kamishima, T. Sasaki, K. Shintani, H. Takegahara, T. Wakizono, and M. Sugiki, Vacuum **83**, 72 (2008).
[25]E. L. Antonsen, R. L. Burton, G. A. Reed, and G. G. Spanjers, Rev. Sci. Instrum. **77**, 103107 (2006).
[26]M. A. Kemp and S. D. Kovaleski, J. Appl. Phys. **100**, 113306 (2006).
[27]M. A. Kemp and S. D. Kovaleski, IEEE Trans. Plasma Sci. **36**, 356 (2008).
[28]Y. Takao and K. Ono, Plasma Sources Sci. Technol. **15**, 211 (2006).
[29]Y. Takao, K. Ono, K. Takahashi, and Y. Setsuhara, Thin Solid Films **506–507**, 592 (2006).
[30]Y. Takao, K. Ono, K. Takahashi, and K. Eriguchi, Jpn. J. Appl. Phys. **45**, 8235 (2006).
[31]Y. Takao, K. Eriguchi, and K. Ono, J. Appl. Phys. **101**, 123307 (2007).
[32]Y. Takao, T. Takahashi, K. Eriguchi, and K. Ono, Pure Appl. Chem. **80**, 2013 (2008).
[33]T. Takahashi, Y. Takao, K. Eriguchi, and K. Ono, J. Phys. D: Appl. Phys. **41**, 194005 (2008).
[34]T. Takahashi, Y. Takao, K. Eriguchi, and K. Ono, Phys. Plasmas **16**, 083505 (2009).
[35]M. Tuda and K. Ono, J. Vac. Sci. Technol. A **16**, 2832 (1998).
[36]M. Tuda, K. Ono, H. Ootera, M. Tsuchihashi, M. Hanazaki, and T. Komemura, J. Vac. Sci. Technol. A **18**, 840 (2000).
[37]H. Kousaka and K. Ono, Jpn. J. Appl. Phys. **41**, 2199 (2002).
[38]H. Kousaka and K. Ono, Plasma Sources Sci. Technol. **12**, 273 (2003).
[39]M. A. Kurtz, T. Gölz, H. Habiger, F. Hammer, H Kurtz, M. Riehle, and C. Sleziona, J. Propul. Power **14**, 764 (1998).
[40]W. A. Hargus, Jr., J. H. Schilling, Q. E. Walker, and M. A. Cappelli, J. Spacecr. Rockets **41**, 1016 (2004).
[41]K. Kinefuchi, I. Funaki, and K. Toki, J. Propul. Power **22**, 1085 (2006).
[42]Note that there is a misprint in the conservation equation for plasma electrons in the previous paper (Ref. 34). The first term on the right-hand side of Eq. (11) in Ref. 34 should be replaced by $\nabla \cdot (D_a \nabla n_e)$.
[43]NIST Standard Database 134, "*Database of the Thermophysical Properties of Gases Used in the Semiconductor Industry*," (http://www.nist.gov/pml/process/fluid/srd_134_gasesindex.cfm)
[44]G. A. Bird, *Molecular Gas Dynamics and the Direct Simulation of Gas Flows* (Clarendon, Oxford, UK, 1994), Chap. 3, p. 69.
[45]J. Jonkers, L. J. M. Selen, J. A. M. van der Mullen, E. A. H. Timmermans, and D. C. Schram, Plasma Sources Sci. Technol. **6**, 533 (1997).
[46]R. W. Crompton, M. T. Elford, and A. G. Robertson, Aust. J. Phys. **23**, 667 (1970).
[47]Y. Sakai, Appl. Surf. Sci. **192**, 327 (2002).
[48]J. W. Shon and M. J. Kushner, J. Appl. Phys. **75**, 1883 (1994).
[49]X. Yuan and L. L. Raja, IEEE Trans. Plasma Sci. **31**, 495 (2003).
[50]T. Belmonte, R. P. Cardoso, G. Henrion, and F. Kosior, J. Phys. D: Appl. Phys. **40**, 7343 (2007).
[51]D. Ton-That, S. T. Manson, and M. R. Flannery, J. Phys. B: Atom. Mol. Phys. **4**, 621 (1977).
[52]D. Ton-That and M. R. Flannery, Phys. Rev. A **15**, 517 (1977).
[53]D. Margreiter, H. Deutsch, and T. D. Mark, Contrib. Plasma Phys. **30**, 487 (1990).
[54]S. Yoon and A. Jameson, AIAA J. **26**, 1025 (1988).
[55]M. A. Lieberman and A. J. Lichtenberg, *Principles of Plasma Discharges and Materials Processing*, 2nd ed. (Wiley, New York, 2005), Chap. 13, p. 530.
[56]G. P. Sutton and O. Biblarz, *Rocket Propulsion Elements* (Wiley, New York, 2001), Chap. 3.
[57]H. W. Liepmann and A. Roshko, *Elements of Gas Dynamics* (Wiley, New York, 1957), Chap. 2.
[58]G. Wirsig, in *Space Propulsion Analysis and Design*, edited by R. W. Humble, G. N. Henry, and W. J. Larson (McGraw-Hill, New York, 1995), Chap. 3.
[59]H. R. Griem, *Plasma Spectroscopy* (McGraw-Hill, New York, 1964), Chap. 4.
[60]H. R. Griem, *Spectral Line Broadening by Plasmas* (Academic, New York, 1974), Chap. III and Appendix I.
[61]Q. Wang, I. Koleva, Y. M. Donnelly, and D. J. Economou, J. Phys. D: Appl. Phys. **38**, 1690 (2005).